Eur. Phys. J. Plus (2025) 140:649
https://doi.org/10.1140/epjp/s13360-025-06579-4

THE EUROPEAN PHYSICAL JOURNAL PLUS

Regular Article

Coil failure effect in geomagnetic field compensation for particle detectors

Sara R. Cabo[1,2,3,a], **J. M. Maco**[2,3,b], **Sergio Luis Suárez Gómez**[3,4,c], **Laura Bonavera**[1,2,d], **Maria Luisa Sanchez**[1,2,e], **Jesús Daniel Santos**[1,2,f], **Francisco Javier de Cos**[2,3,g]

[1] Departamento de Física, Universidad de Oviedo, Calvo Sotelo 18, 33007 Oviedo, Asturias, Spain
[2] MOMA, Instituto Universitario de Ciencias y Tecnologías Espaciales de Asturias (ICTEA), Independencia 13, 33004 Oviedo, Asturias, Spain
[3] Departamento de Explotación y prospección de Minas, Universidad de Oviedo, Independencia 13, 33004 Oviedo, Asturias, Spain
[4] Departamento de Matemáticas, Universidad de Oviedo, Calvo Sotelo 18, 33007 Oviedo, Asturias, Spain

Received: 21 March 2025 / Accepted: 21 June 2025

Abstract Photomultiplier tubes (PMTs) in large Cherenkov detectors suffer from efficiency loss due to the Earth's geomagnetic field, which alters electron trajectories. Active compensation using current-carrying coils is an effective solution but is susceptible to failures that can compromise the homogeneity of the compensated field and degrade detector performance. This study systematically analyzes the impact of individual coil failures on geomagnetic compensation, focusing on key evaluation parameters: the proportion of PMTs exposed to residual perpendicular magnetic field exceeding acceptable limits (P_{100}) and the average residual perpendicular field ($< B_{\text{perp}} >$). Furthermore, a fail-safe connection system utilizing multi-core cables and external reconnection points is introduced, mitigating the effects of coil malfunctions and ensuring more stable long-term performance of large-scale detectors.

1 Introduction

Neutrinos, among the most abundant particles in the universe, play a pivotal role in both particle physics and astrophysics. Their weak interaction with matter renders them invaluable probes for studying cosmic phenomena and fundamental forces. However, this property poses a significant challenge for their detection, driving the development of increasingly sophisticated experiments. Neutrino studies have led to groundbreaking discoveries, from the confirmation of their oscillations and their finite, albeit minuscule, mass [1] to their pivotal role in astrophysical phenomena such as supernovae [2]. Beyond deepening our understanding of these elusive particles, they also offer crucial insights into the evolution of the universe and potential new physics, including proton decay and the nature of dark matter [3].

One of the most prevalent detection techniques is the Cherenkov method, which, rather than directly detecting neutrinos, captures the Cherenkov radiation produced in neutrino interactions [4]. Water is the most common detection medium, although alternative approaches, such as liquid argon detectors, are actively being explored, as exemplified by the DUNE experiment [5]. Large-scale detectors based on this technology play a crucial role in neutrino research, with key experiments including Super-Kamiokande [6], Hyper-Kamiokande [3], JUNO [7], IceCube [8], DUNE [5], KM3NeT [9], Borexino [10], SNO [11] and NOvA [12].

The performance of these detectors is critically dependent on photomultiplier tubes (PMTs), which convert Cherenkov light into electrical signals used to reconstruct neutrino interactions. However, the Earth's geomagnetic field induces inefficiencies in PMTs: as it perturbs the trajectories of photoelectrons within the tubes, thereby diminishing their effective sensitivity [13]. Several mitigation strategies have been proposed, including passive shielding with μ-metal [14]. While effective, this material has certain drawbacks, such as structural rigidity, potential radioactive contamination [15] and the presence of residual magnetic fields that can still impact PMT performance [16]. It is also static and cannot dynamically adjust to changing magnetic field conditions over time.

A commonly considered alternative, particularly in certain large-scale detectors, is active magnetic field compensation through current-carrying coils. This method involves surrounding the detector with conductive coils that generate a magnetic field opposing the Earth's field. By adjusting the current in these coils, the residual field inside the detector can be significantly reduced, in some

[a] e-mail: rodriguezcsara@uniovi.es (corresponding author)
[b] e-mail: menendezjimena@uniovi.es
[c] e-mail: suarezsergio@uniovi.es
[d] e-mail: bonaveralaura@uniovi.es
[e] e-mail: mlsr@uniovi.es
[f] e-mail: jdsantos@uniovi.es
[g] e-mail: fjcos@uniovi.es

Published online: 10 July 2025

cases reaching levels lower than those achievable with μ-metal shielding alone [16]. Moreover, active compensation allows for dynamic adjustments if environmental conditions change. However, this approach also presents several challenges: It requires a stable power supply, careful design to avoid interference with maintenance operations and a mechanically robust infrastructure capable of supporting the coils. Furthermore, this technique is not applicable to all experiments mentioned earlier, such as KM3NeT or IceCube, where the experimental environment or geometry renders coil-based compensation unfeasible.

Among these practical considerations, an important yet less examined issue arises: the impact of coil failures on the uniformity of the compensated magnetic field. Unlike μ-metal shielding, which remains effective regardless of electrical configuration, active compensation relies on precise electrical operation. Interruptions in the power supply, partial disconnections or installation defects could compromise field uniformity, potentially affecting PMT performance.

A relevant example of such a failure was observed in Super-Kamiokande, where a coil failed in three locations due to what is believed to be a manufacturing defect. Over time, cable deterioration allowed water **infiltration**, ultimately disrupting the coil's functionality. In consequence a 10–20% of detection efficiency loss was observed in around 20% of PMTs. This incident underscores the potential vulnerabilities of coil-based compensation systems and the importance of designing robust and fault-tolerant configurations [19].

Understanding the consequences of such failures is crucial to ensuring long-term detector stability and optimizing performance [17, 20]. This work focuses on analyzing the effects of coil failures on magnetic field compensation, assessing their impact on the compensation common evaluation parameters and establishing criteria to mitigate potential disruptions.

The first section outlines the objectives of this study, the experimental design and the methodology used for the simulations. The following section presents the results, analyzing how the effectiveness of geomagnetic field compensation deteriorates as a function of various parameters when coil failures occur. Subsequently, a strategy to mitigate the impact of potential coil malfunctions is proposed. Finally, the conclusions and key findings of this work are summarized.

2 Objectives and experiment design

2.1 Objectives

The efficiency of a geomagnetic field compensation system is susceptible to the failure of one or more coils, resulting in a rise in the residual perpendicular magnetic field experienced by the photomultiplier tubes (PMTs). In previous studies [17, 18], key parameters influencing the effectiveness of the system, such as the spacing between coils, the distance between PMTs and coils and the overall detector size, have been established as critical factors.

This study aims to analyze the impact of coil failures on the evaluation metrics of the compensation system, particularly the proportion of PMTs exposed to more than 100 mG of perpendicular residual magnetic field (P_{100}) and the average perpendicular magnetic field ($< B_{\text{perp}}$). These are two commonly considered parameters that have been proven to describe complementary aspects of geomagnetic field compensation and loss of detection efficiency [18]. While $< B_{\text{perp}} >$ is used as the main evaluation metric, the standard deviation is also considered in all analyses to account for field non-uniformities. A large dispersion in the residual field across the detector would indicate regions with suboptimal compensation, which could introduce detector-related uncertainties. Therefore, both the mean and the spread of $< B_{\text{perp}} >$ are relevant to assess the overall robustness of the magnetic field compensation.

By systematically studying how these metrics are affected by coil failures under different geometric and design conditions, the objective is to characterize the system's robustness and identify configurations that minimize performance degradation.

Based on this analysis, an optimized connection scheme will be proposed for the compensation coils that reduces the negative effects of a potential failure. The goal is to ensure that, even in the event of a coil malfunction, the system maintains a compensation performance as close as possible to the optimal configuration, enhancing the reliability and stability of the detector's magnetic environment.

2.2 Design of the system

The detector is conceptualized as a cylindrical structure, with its center which serves as the origin of the coordinate system adopted in this study, as illustrated in Fig. 1. In this reference frame, the Z-axis is oriented vertically, while the X- and Y-axes lie in the horizontal plane. The geomagnetic field at any point within the detector volume is represented as a three-dimensional vector field.

The compensation system consists of two sets of coils along the inner surface of the detector, aligned with the components of the geomagnetic field. When an appropriately optimized current flows through these coils, it generates a magnetic field opposing that of the Earth, thereby mitigating its influence. However, the magnetic field produced by the coils is not uniform throughout the detector volume. Factors such as the finite dimensions of the coils, edge effects and the overall geometry contribute to spatial variations in the generated field. Consequently, the residual magnetic field experienced by each PMT depends on its position. The optimized current values are chosen to minimize the overall impact of the residual magnetic field across the detector, as quantified by parameters such as P_{100} and $< B_{\text{perp}} >$ rather than achieving a uniform field throughout the tank.

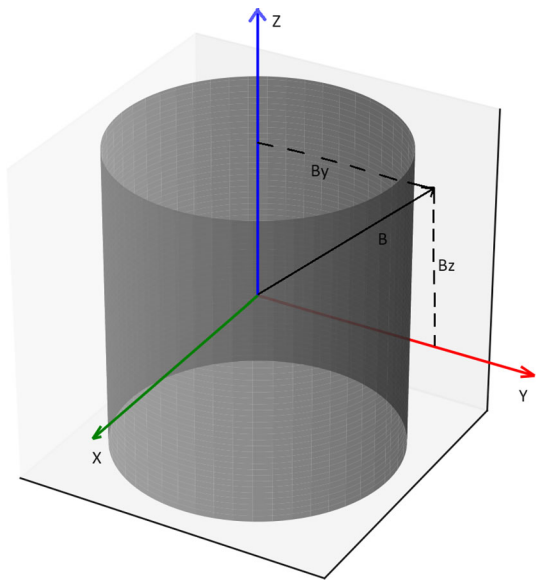

Fig. 1 Schematic representation of the generic cylindrical detector under consideration. The reference system used is also shown, with origin at the center of the detector, as well as an example of a geomagnetic field vector

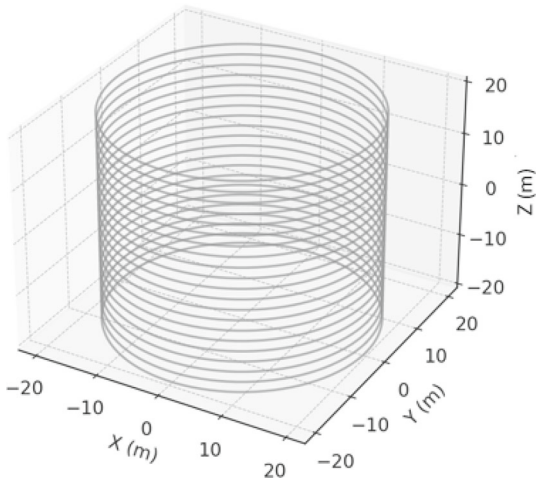

Fig. 2 Simulation of circular coil system centered on Z-axis for geomagnetic field compensation in a tank of 40 m height and diameter

To simplify the system and avoid the need for three independent coil sets—one for each geomagnetic field component—the X component of the field is mathematically set to zero. This adjustment is not achieved by physically rotating the detector or the coils, but by defining a coordinate system centered on the detector and rotating this system within the XY plane. This transformation effectively nullifies the X component of the geomagnetic field in the chosen frame of reference. In the specific case of a cylindrical detector with coils installed along the inner surface of the tank, this choice of coordinate system does not impose practical constraints, as the coil placement is not obstructed and can be oriented arbitrarily in the horizontal plane. Therefore, the mathematical simplification adopted here is compatible with realistic implementation in this geometry. Nevertheless, in experiments with different geometries or constraints, such freedom may not be available, and the feasibility of aligning the coordinate system in this manner would need to be assessed on a case-by-case basis.

As a result, only two coil sets are required for compensation. Given the cylindrical geometry of the detector, one set consists of circular coils centered on the Z-axis to counteract the vertical component B_Z, as illustrated in Fig. 2. The second set consists of rectangular coils centered on the Y-axis to compensate for the nonzero horizontal component B_Y, as shown in Fig. 3.

These coils are installed along the inner surface of the detector. The circular coils match the radius of the tank and are equally distributed between top and bottom. The rectangular coils, on the other hand, are circumscribed, meaning their height is equal to that of the detector, while their horizontal length varies depending on the radius. For this study, standard conductive (non-superconducting) coils are considered. The optimal number of coils in each set depends on the specific dimensions of the detector, as extensively analyzed in [17].

To determine the residual magnetic field at each PMT, it is necessary to specify their precise positions. In this study, PMTs with a 50 cm diameter are used, following advanced models designed for high-energy physics applications in large-scale Cherenkov detectors [21], such as the Hamamatsu R12860 and R3600 employed in the Super-Kamiokande neutrino detector [22]. The distance between the centers of adjacent PMTs is set to 70 cm.

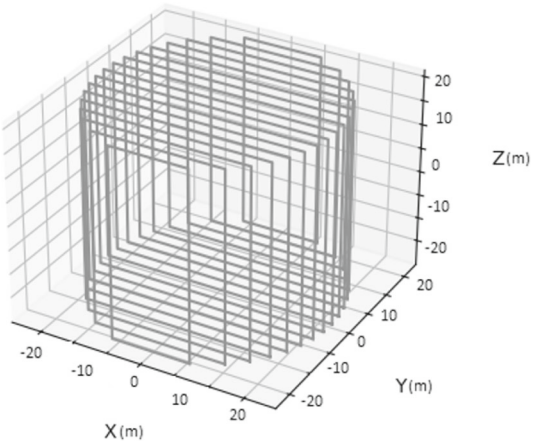

Fig. 3 Simulation of rectangular coil system centered on Y-axis for geomagnetic field compensation in a tank of 40 m height and diameter

The PMTs are mounted on frames within the detector, forming an inner cylindrical array. It is important to emphasize that the coils are fixed to the tank's inner surface, meaning that adjusting the distance between PMTs and coils effectively alters the size of the inner detection cylinder. Increasing this distance reduces the effective detection volume. The gaps between adjacent PMTs are covered with opaque black foils to absorb stray radiation. These foils do not influence the magnetic field simulation and are treated as empty spaces in the analysis [3, 22].

The simulation assumes that the geomagnetic field at the detector site has been well characterized through prior detailed studies, ensuring an accurate understanding of its magnitude and direction. While the coils are assumed to be aligned accordingly, certain practical factors may introduce slight misalignments. Local magnetic anomalies, installation tolerances or geomagnetic fluctuations could cause minor deviations. Although these variations are expected to have a limited effect on the overall compensation strategy, they are acknowledged as potential sources of discrepancy in the simulation results. Nevertheless, the conclusions drawn remain valid within the scope of this study.

2.3 Calculation of total and perpendicular magnetic field

The total residual magnetic field at each PMT arising from the interaction of the geomagnetic field and the compensating coils is computed as follows. The residual field, denoted as $B_{\text{total}} = (\Delta B_X,\ \Delta B_Y,\ \Delta B_Z)$, is given by:

$$B_{\text{total}} = (B_{X_{\text{geo}}} + B_{X_{\text{coils}}}, B_{Y_{\text{geo}}} + B_{Y_{\text{coils}}}, B_{Z_{\text{geo}}} + B_{Z_{\text{coils}}}) \tag{1}$$

In other words, at each PMT location, the total residual field is obtained by summing the geomagnetic field and the field induced by the coils. The magnitude of this field is given by:

$$B_{\text{total}} = \sqrt{\Delta B_X^2 + \Delta B_Y^2 + \Delta B_Z^2} \tag{2}$$

Since the reference frame has been defined so that the geomagnetic field has no $B_{X_{\text{geo}}}$ component, only the coils generate a field in this direction. However, simulations indicate that the magnetic field in this component is an order of magnitude smaller than that in the other two directions, as the coils are not specifically optimized for this axis. Although this effect must be considered, it is not expected to significantly impact the overall compensation strategy.

Another key parameter in assessing compensation performance is the residual magnetic field perpendicular to the PMTs, denoted as B_{perp}. The efficiency of PMTs is most adversely affected by magnetic fields oriented perpendicular to their axis, as these fields disrupt electron trajectories. The parameter B_{perp} isolates the perpendicular field component responsible for efficiency degradation, disregarding the parallel component, which has a negligible effect unless its magnitude is substantially higher.

The calculation of B_{perp} presents additional complexities due to the varying orientation of PMTs relative to the reference frame, dictated by their placement within the detector. Figure 4 illustrates the orientations of PMTs on the walls and lids.

Different expressions are derived for B_{perp} depending on whether the PMTs are mounted on the cylindrical walls or the top and bottom lids. The expression for PMTs on the side walls is given by:

$$B_{\text{perp}}^{\text{walls}} = \sqrt{(\Delta B_X \cdot \sin\theta + \Delta B_Y \cdot \cos\theta)^2 + \Delta B_Z^2} \tag{3}$$

where θ represents the angle between the PMT axis and the Y-axis. Figure 5 illustrates the decomposition of the horizontal magnetic field component as a function of this angle.

This expression accounts for only the components of ΔB_X and ΔB_Y perpendicular to the PMT axis, while the entire ΔB_Z component contributes, as it is always perpendicular to the horizontally mounted PMTs on the walls. The expression for the

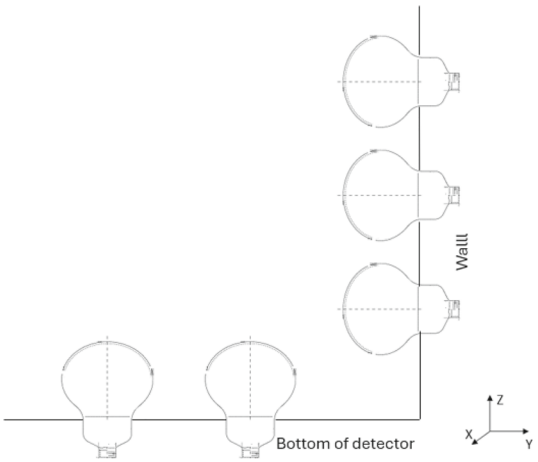

Fig. 4 Orientation of PMTs in a cylindrical detector. The orientation depends on whether they are on the lids or on the walls. The XYZ system of reference is also depicted

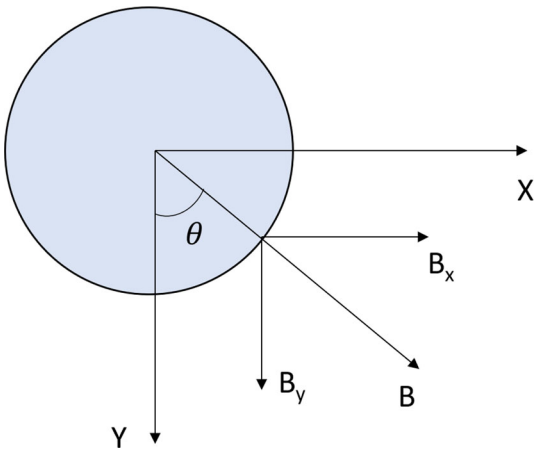

Fig. 5 Decomposition of the magnetic field at a generic point on the surface of the detector into its various components

perpendicular field on the lid PMTs follows a similar derivation. In this case, the B_Z component has no contribution as it is parallel to the axis of the PMTs at the lids.

$$B_{\text{perp}}^{\text{lids}} = \sqrt{\Delta B_X^2 + \Delta B_Y^2} \tag{4}$$

To calculate the magnetic field created by each coil at the exact position of each PMT, the Biot-Savart law is applied within the framework of Maxwell's classical theory of electromagnetism.

2.4 Design of the experiment

The performance of a geomagnetic field compensation system is highly susceptible to coil failures, which induce variations in the residual perpendicular magnetic field experienced by the PMTs. The severity of this effect is contingent upon several geometric and design parameters, as established in [17], including coil spacing, the distance between PMTs and coils, and overall detector size.

To systematically study this effect, simulations are performed to analyze how coil failures influence the evaluation metrics of the compensation system, with a focus on the proportion of PMTs subjected to perpendicular residual magnetic fields exceeding 100 mG of perpendicular residual magnetic field (P_{100}) and the average perpendicular magnetic field ($< B_{\text{perp}} >$). The goal is to determine how these parameters evolve in response to failures across varying geometric configurations and whether targeted design modifications can mitigate the loss of compensation efficiency.

Initially, the response of P_{100} and $< B_{\text{perp}} >$ is examined as a function of coil spacing, PMT-to-coil distance, detector size and the type of coil set (circular or rectangular) affected by the failure, in accordance with the methodology outlined in [17]. This analysis facilitates a more comprehensive assessment of how these factors govern the system's resilience to coil failures.

Subsequently, a practical coil system configuration is devised, wherein coils are arranged into multiple sets, each powered by an independent supply. Should a failure occur within one of these sets, multiple coils would be disconnected simultaneously, potentially compromising the compensation field. The worst-case scenario is evaluated, and an alternative wiring scheme is introduced to ensure partial current continuity, thereby mitigating detrimental effects on system performance.

The detector sizes considered in this study are $h = D = 40\,\text{m}$ and $h = D = 60\,\text{m}$. The simulated geomagnetic field corresponds to intermediate latitudes, with both components equal: $B_{\text{geo}} = 475\,\text{mG}$, with $B_{Y_{\text{geo}}} = B_{Z_{\text{geo}}} = 335.88\,\text{mG}$. The influence of detector size, geometry and different geomagnetic field values on compensation has been extensively studied in [17].

2.5 Simulation

The simulation framework for geomagnetic field compensation in the detector comprises three Python modules. The first module defines the coil geometry, encompassing circular, rectangular, and, in specific cases, elliptical configurations. The second module computes the magnetic field generated by the coils at any given coordinate through direct application of Biot-Savart's law.

The *third and main module makes use of the preceding two components* and defines key detector parameters, including its dimensions and the precise locations of the PMTs. This module encompasses three principal functions. The core function establishes the spatial configuration and current parameters of the coils. It then computes the total magnetic field as the sum of the geomagnetic field and the field induced by all coils, decomposed into its components. Additionally, it determines the perpendicular magnetic field at each PMT axis. Finally, the function outputs the mean total and perpendicular magnetic fields within the detector, alongside the proportion of photomultipliers subjected to perpendicular magnetic fields exceeding 100 mG.

The second function produces a histogram depicting the distribution of the perpendicular magnetic field and a graphical representation of the cylindrical tank, identifying the locations of photomultipliers where the residual perpendicular magnetic field surpasses 100 mG. The third function employs a genetic algorithm to optimize the current intensity applied to the coils.

A genetic algorithm is an optimization technique inspired by genetic processes and natural selection, designed to solve nonlinear multivariate problems [23]. It begins with a population of N individuals, each represented by a chromosome. Each chromosome consists of a set of genes, corresponding to the parameters being optimized. For a system with nn parameters, each chromosome contains nn values—one for each parameter. In this application, the genes represent the current intensity through the circular and rectangular coils. For simplicity and cost efficiency, all coils of the same geometry are assumed to carry the same current intensity.

A key component of the algorithm is the fitness function, which evaluates the effectiveness of each chromosome as a solution to the problem. In this case, the fitness function is the program that calculates the residual perpendicular magnetic field at the PMT locations, returning the number of PMTs exposed to less than 100 mG. The goal is to maximize this number.

3 Results

3.1 Influence of Coil Spacing

This section analyzes the effects of coil failures on geomagnetic compensation, with a focus on key evaluation parameters such as the proportion of PMTs subjected to more than 100 mG of residual perpendicular magnetic field (P_{100}) and the mean residual perpendicular magnetic field across all PMTs ($< B_{\text{perp}} >$).

The variations in these parameters resulting from individual coil failures are examined, where a failure is defined as a disruption in the current flow through the affected coil. This study considers both circular and rectangular coils, evaluating two representative detector sizes and different coil spacing values, denoted as d_C, to assess their influence on the extent of these variations. The study first examines the baseline coil configurations. Subsequently, the potential benefits of incorporating additional circular coils at the upper and lower ends of the tank, as proposed in [17], are examined. Furthermore, the impact of varying the distance between the coils and PMTs, denoted as d_W, is explored.

For all configurations, the same current is applied to all circular coils and to all rectangular coils. This current is set to the value that optimizes the evaluation parameters (P_{100} and $< B_{\text{perp}} >$) in each case, as determined in the simulation methodology described in the previous section.

Figures 6, 7, 8 and 9 illustrate the impact of individual coil failures within the geomagnetic field compensation system of a detector with dimensions $h = D = 40\,\text{m}$. The distance between coils and PMTs is fixed at an intermediate reference value of $d_W = 2\,\text{m}$. In this way it is possible to compare, on the one hand, the effect on the compensation of a failure in the circular and rectangular coils. At the same time, by fixing the value of d_W and varying the value of the distance between coils d_C, the effect on the impact of the latter parameter can be evaluated.

In addition, Table 1 provides the values of both evaluation parameters corresponding to the basic configuration of coils without any failure for each value of the distance between coils.

First, comparing the increase in P_{100} in rectangular and circular coils by means of the graphs 6 and 7, a key observation is that the value of P_{100} gets higher as the distance between coils d_C increases in both cases. This is expected since the more separated the coils are, if one of them fails, the gap between the one before and the one after becomes noticeably larger, which translates into a non-negligible portion of the detector being not properly compensated.

Moreover, it can be observed that the failure of a rectangular coil has a greater impact on the compensation than that of a circular coil, which is especially evident for large values of d_C. For such values, represented here by $d_C = 4\,\text{m}$ and $d_C = 5\,\text{m}$, this trend is

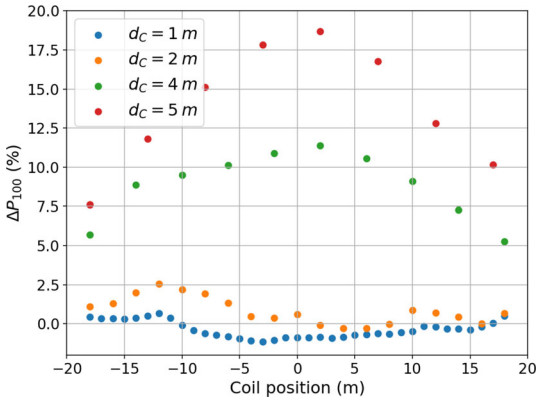

Fig. 6 Increase in P_{100} with the failure of each of the rectangular coils of the compensation system of a detector of $h = D = 40\,\text{m}$ and $d_W = 2\,\text{m}$ for different values of the distance between coils d_C

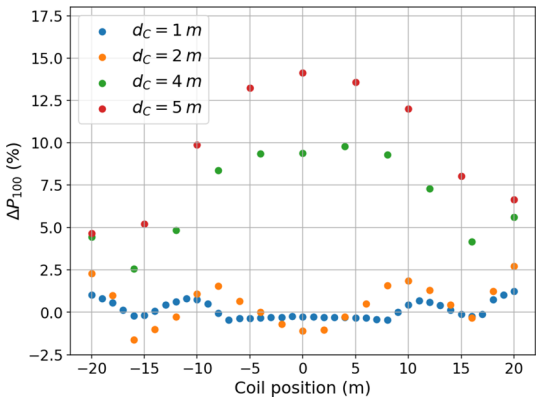

Fig. 7 Increase in P_{100} with the failure of each of the circular coils of the compensation system of a detector of $h = D = 40\,\text{m}$ and $d_W = 2\,\text{m}$ for different values of the distance between coils d_C

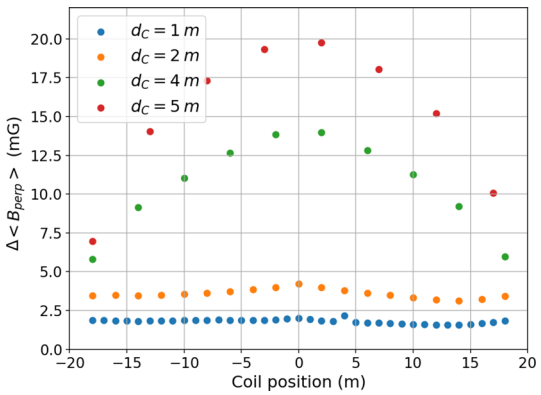

Fig. 8 Increase in $< B_{\text{perp}} >$ with the failure of each of the rectangular coils of the compensation system of a detector of $h = D = 40\,\text{m}$ and $d_W = 2\,\text{m}$ for different values of the distance between coils d_C

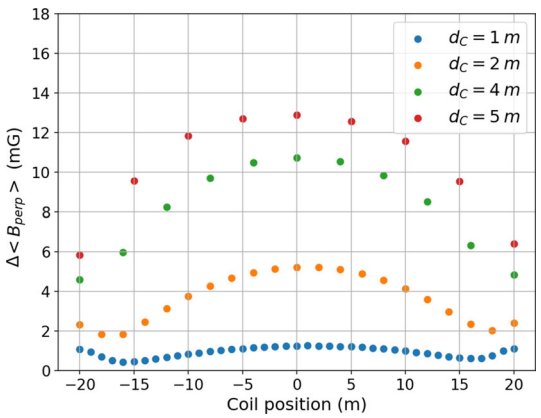

Fig. 9 Increase in $< B_{\text{perp}} >$ with the failure of each of the circular coils of the compensation system of a detector of $h = D = 40\,\text{m}$ and $d_W = 2\,\text{m}$ for different values of the distance between coils d_C

Table 1 Values of P_{100} and $< B_{\text{perp}} >$ of a basic configuration of coils for a detector with $h = D = 40$ m and $d_W = 2$ m

d_C	$P_{100}(\%)$	$< B_{\text{perp}} > (mG)$
1 m	12.83	57.82
2 m	12.11	54.84
4 m	9.85	58.12
5 m	12.83	66.07

Table 2 Values of P_{100} and $< B_{\text{perp}} >$ of a basic configuration of coils for a detector with $h = D = 60$ m and $d_W = 2$ m

d_C	$P_{100}(\%)$	$< B_{\text{perp}} >$ (mG)
1 m	17.31	61.65
2 m	16.28	60.55
4 m	15.86	65.16
5 m	19.41	72.87

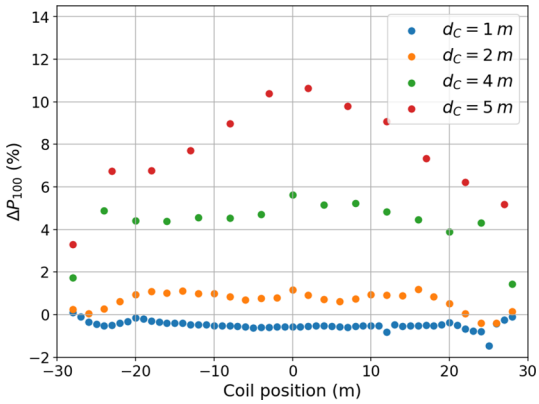

Fig. 10 Increase in P_{100} with the failure of each of the rectangular coils of the compensation system of a detector of $h = D = 60$ m and $d_W = 2$ m for different values of the distance between coils d_C

clearly observed. The greatest negative impact on geomagnetic field compensation occurs when a failure affects the central coils, both circular and rectangular. This effect diminishes symmetrically toward the edges.

In contrast, for lower values, such as $d_C = 1$ m and $d_C = 2$ m, the behavior of P_{100} after a failure is more uniform and remains consistently low. Peaks are also observed around a quarter of the detector's dimension. These low-coil-spacing cases are of particular interest because, after simulating failures in specific coils, P_{100} decreases instead of increasing. This suggests that removing these coils from the design could be advantageous if the primary objective is to minimize this parameter. This occurs because, in these particular cases, the coil density is such that the field may become overcompensated.

In Figures 8 and 9, a similar representation is provided, but in this case, it depicts the effect of coil failures on $< B_{\text{perp}} >$. Once again, the results indicate that the effect of a failure on the compensation is more pronounced as the distance between coils d_C increases, for both rectangular and circular coils. In these cases, the trend is much clearer, with the maximum increase in $< B_{\text{perp}} >$ occurring in the central coils in all cases except for $d_C = 1$ m. This particular scenario, characterized by greater uniformity due to the density of coils over the whole detector, also shows maximum values when the failure occurs in the circular coils at the extremes.

Once again, the impact of a rectangular coil failure is more detrimental than that of a circular coil, especially when the system is designed with a large coil spacing. A comparison between the impact on $< B_{\text{perp}} >$ and P_{100} reveals that $< B_{\text{perp}} >$ increases with the failure of any coil in all cases, unlike P_{100}, which was previously shown to potentially decrease if certain coils failed. However, regarding $< B_{\text{perp}} >$, compensation consistently deteriorates following a failure.

To analyze the effect of detector size, the same coil failure simulations are repeated for a detector with $h = D = 60$ m. In [17], a larger detector size has been shown to complicate compensation. This trend is also reflected in the evaluation parameters of the baseline case without failures, as shown in 2. Figures 10, 11, 12 and 13 present the increase in both P_{100} and $< B_{\text{perp}} >$ following the failure of each coil for different values of d_C, while keeping the distance between PMTs and coils fixed at $d_W = 2$ m for this larger detector.

A comparison with the figures for a 40-m detector reveals that the behavior is fully analogous in all cases. However, the main distinction with a larger detector is that, regardless of the coil spacing or whether the coils are rectangular or circular, the impact of a failure on the compensation is reduced. For example, the failure of the central circular coil in a detector of 40 m with $d_C = 5$ m leads to an increase of 14.14% for P_{100} and 12.89 mG for $< B_{\text{perp}} >$. Under the same conditions, but for a 60-m detector, it leads to an increase of 7.95% for P_{100} and of 7.56 mG for $< B_{\text{perp}} >$. This confirms that geomagnetic field compensation becomes more challenging as detector size increases, while, conversely, the impact of coil failures is reduced.

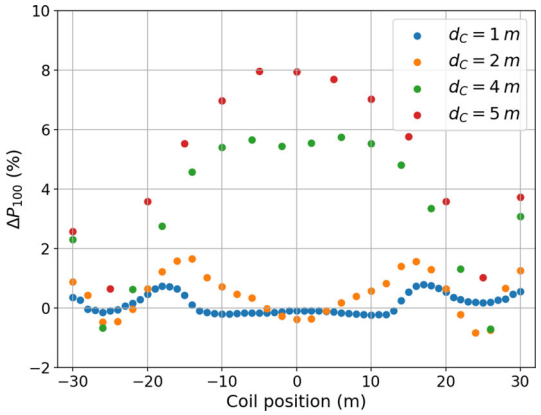

Fig. 11 Increase in P_{100} with the failure of each of the circular coils of the compensation system of a detector of $h = D = 60$ m and $d_W = 2$ m for different values of the distance between coils d_C

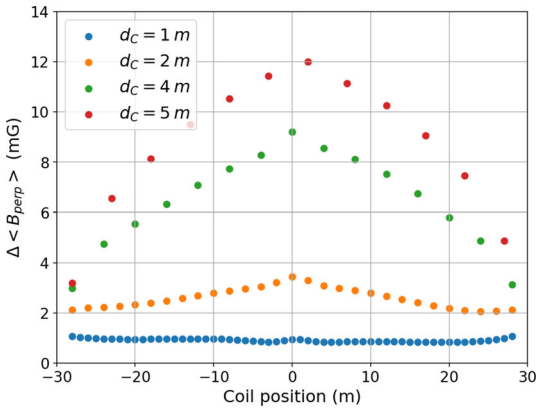

Fig. 12 Increase in $< B_{\text{perp}} >$ with the failure of each of the rectangular coils of the compensation system of a detector of $h = D = 60$ m and $d_W = 2$ m for different values of the distance between coils d_C

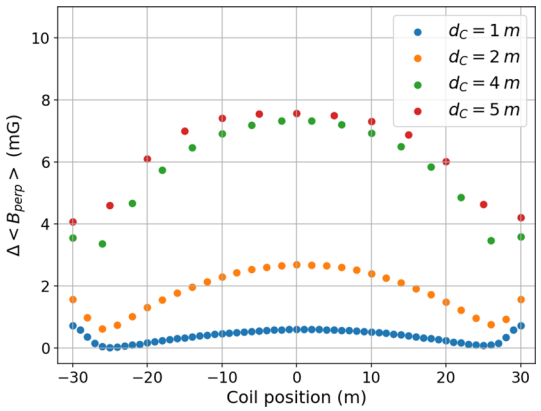

Fig. 13 Increase in $< B_{\text{perp}} >$ with the failure of each of the circular coils of the compensation system of a detector of $h = D = 60$ m and $d_W = 2$ m for different values of the distance between coils d_C

3.2 Failure in optimized design

So far, the effect of coil failure has been analyzed in a basic compensation system consisting of rectangular and circular coils spaced separated by a specific distance and carrying a uniform current. Here, this is termed a basic coil-based compensation system. However, as demonstrated in [17], further improvements in compensation can be attained by increasing the magnetic field density generated in the upper and lower areas of the detector. In particular, the top and bottom edges of the tank walls have been identified as the most challenging regions for effective compensation.

In order to generate a higher magnetic field with locally shaped coils in these areas without significantly impacting the rest of the detector, the addition of a higher number of turns to the circular coils at the top and bottom edges has been successfully tested. The addition of circular coils in these positions but with a smaller radius has also been particularly effective in decreasing the $< B_{\text{perp}} >$ value. These new coils would carry the same current as the other circular ones to simplify the system and reduce the number of power supplies. Once incorporated, the optimal current requires slight adjustment. This approach has proven to be the most effective in compensating for the Earth's magnetic field in the most challenging regions of detectors with this geometry, according to previous related studies [17, 18].

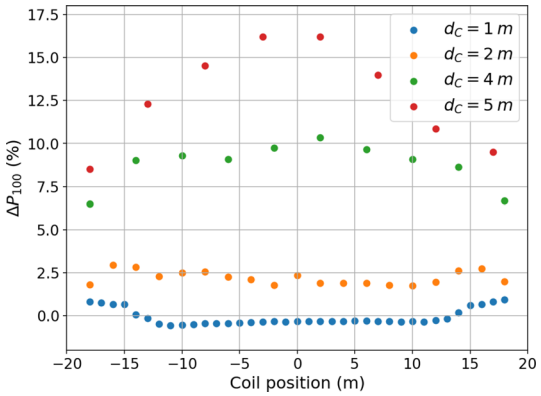

Fig. 14 Increase in P_{100} with the failure of each of the rectangular coils of the optimized compensation system of a detector of $h = D = 40$ m and $d_W = 2$ m for different values of the distance between coils d_C

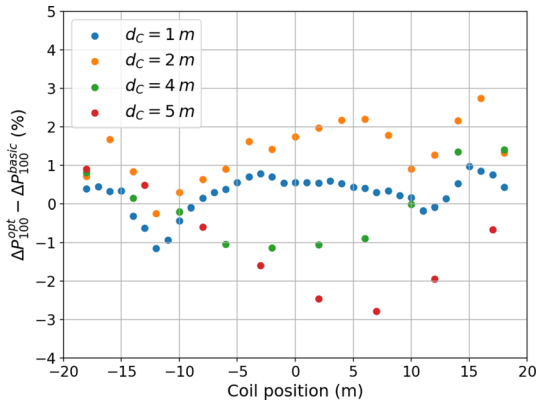

Fig. 15 Difference in the increase in P_{100} after the failure of each individual rectangular coil between the optimized and the basic configurations for a detector of $h = D = 40$ m and $d_W = 2$ m for different values of the distance between coils d_C

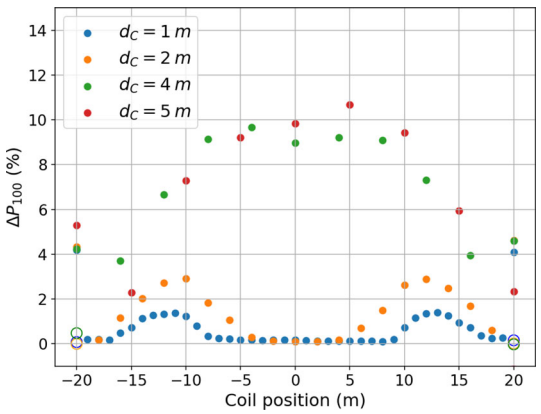

Fig. 16 Increase in P_{100} with the failure of each of the circular coils of the optimized compensation system of a detector of $h = D = 40$ m and $d_W = 2$ m for different values of the distance between coils d_C. The smaller additional coils are represented with unfilled circles

Table 3 Values of P_{100} and $< B_{\text{perp}} >$ of the optimized configuration of coils for a detector with $h = D = 40$ m and $d_W = 2$ m

d_C	P_{100}(%)	$< B_{\text{perp}} >$ (mG)
1 m	4.66	45.36
2 m	3.77	39.43
4 m	4.94	46.31
5 m	12.18	60.56

By changing the arrangement of the coils in this optimized case, the impact of a coil failure is also expected to change. In order to assess this, the increase in both evaluation parameters resulting from coil failures of the individual coils is simulated again, considering various values of the coil spacing, d_C. As an example, Figs. 14, 16, 18 and 20 show the results for a detector of intermediate size, h = D = 40 m and with the distance between coils and PMTs set to $d_W = 2$ m.

On the other hand, Table 3 shows the value of the evaluation parameters obtained by the optimized system operating under normal conditions without failure in any of the coils. Figures 15, 17, 19, and 21 show the difference in the impact of a single coil failure on the values of P_{100} and $< B_{\text{perp}} >$ between the optimized and the basic configurations for comparison.

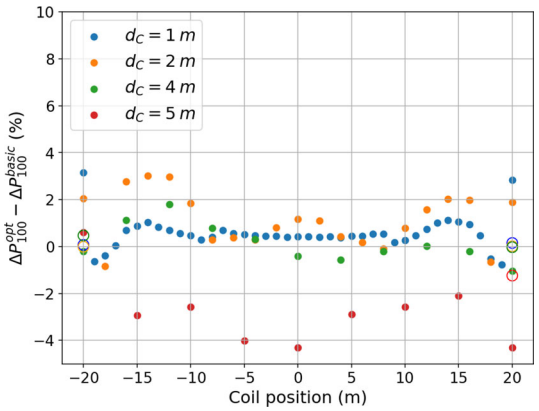

Fig. 17 Difference in the increase in P_{100} after the failure of each individual circular coil between the optimized and the basic configurations for a detector of $h = D = 40\,\text{m}$ and $d_W = 2\,\text{m}$ for different values of the distance between coils d_C. The smaller additional coils are represented with unfilled circles

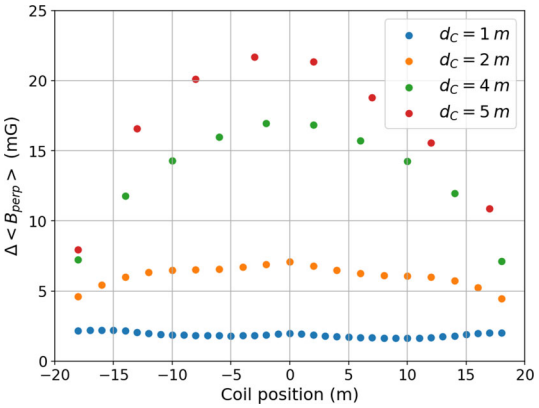

Fig. 18 Increase in $< B_{\text{perp}} >$ with the failure of each of the rectangular coils of the optimized compensation system of a detector of $h = D = 40\,\text{m}$ and $d_W = 2\,\text{m}$ for different values of the distance between coils d_C

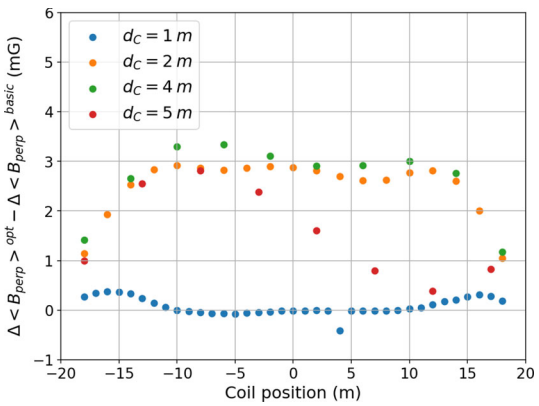

Fig. 19 Difference in the increase in $< B_{\text{perp}} >$ after the failure of each individual rectangular coil between the optimized and the basic configurations for a detector of $h = D = 40\,\text{m}$ and $d_W = 2\,\text{m}$ for different values of the distance between coils d_C

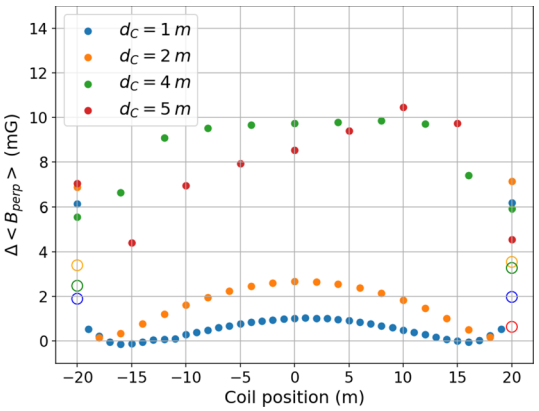

Fig. 20 Increase in $< B_{\text{perp}} >$ with the failure of each of the circular coils of the optimized compensation system of a detector of $h = D = 40\,\text{m}$ and $d_W = 2\,\text{m}$ for different values of the distance between coils d_C. The smaller additional coils are represented with unfilled circles

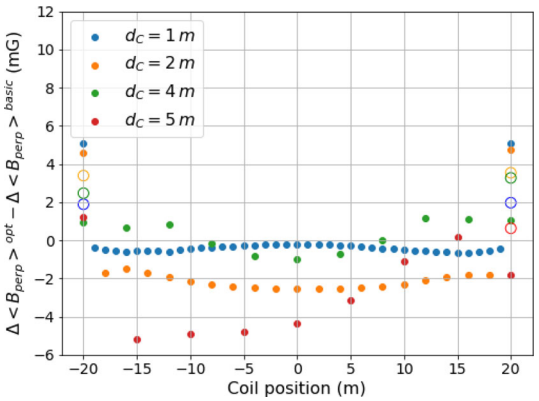

Fig. 21 Difference in the increase in $< B_{\text{perp}} >$ after the failure of each individual circular coil between the optimized and the basic configurations for a detector of $h = D = 40\,\text{m}$ and $d_W = 2\,\text{m}$ for different values of the distance between coils d_C. The smaller additional coils are represented with unfilled circles

Table 4 Impact of the failure of the top and bottom smaller circular coils on the P_{100} and $< B_{\text{perp}} >$ parameters for different values of d_C

d_C (m)	Top		Bottom	
	ΔP_{100} (%)	$\Delta < B_{\text{perp}} >$ (mG)	ΔP_{100} (%)	$\Delta < B_{\text{perp}} >$ (mG)
1	0.15	1.97	0.07	1.89
2	0.01	3.54	−0.01	3.39
4	−0.03	3.27	0.47	2.47
5	−1.24	0.63	–	–

Regarding P_{100}, for rectangular coils, the impact of a failure remains largely unchanged. However, a slight increase in its impact is observed in the central coils when d_C is small, whereas for larger values of d_C, the failure of a rectangular coil has a lower impact in the optimized configuration. This suggests that optimization has a minimal effect on the behavior of rectangular coils under failure conditions, although some variations appear depending on their position and the coil spacing.

For circular coils, more significant differences arise. Unlike in the non-optimized system, no coil failure leads to an improved P_{100} configuration, unlike in the base case. For small coil spacings, such as $d_C = 1\,\text{m}$ and $d_C = 2\,\text{m}$, the largest increase in P_{100} occurs when the upper or lower circular coils fail. However, additional peaks in P_{100} increase are observed when failures occur at intermediate positions.

In general, for low values of d_C, the effect of a failure is more severe than in the basic system, regardless of the affected coil. For larger spacings, ($d_C = 4\,\text{m}$ and $d_C = 5\,\text{m}$), this pattern shifts. In these cases, the most significant impact on P_{100} still arises when the failure affects the central circular coils, similar to the basic configuration.

Regarding $< B_{\text{perp}} >$, the effect of a failure in rectangular coils remains qualitatively consistent with that in in the non-optimized system. However, in this case, the negative impact of a failure increases, regardless of the coil spacing, reaching differences over 3 mG compared to the non-optimized configuration. For circular coils, however, coil position plays a more significant role. The failure of circular coils at extreme positions has a more pronounced negative effect compared to the basic system, while the impact of failures in central circular coils is reduced.

This effect is especially noticeable for small d_C, where the increase in $< B_{\text{perp}} >$ due to failures in extreme-positioned coils is significantly greater. Conversely, for large d_C, the attenuation of $< B_{\text{perp}} >$ increase due to central coil failures becomes more evident.

In the case of failure of the small circular coils, the data displayed in Table 4 reveal a distinct trend in the impact of a coil failure on both P_{100} and $< B_{\text{perp}} >$. The most significant increase in P_{100} occurs when the bottom coil fails, particularly for lower values of d_C, highlighting a stronger sensitivity in the lower region of the detector. Conversely, the impact of a top coil failure remains more moderate across all cases, suggesting a slight asymmetry in how compensation is affected at different vertical positions.

Regarding $< B_{\text{perp}} >$, the failure of either the top or bottom coil leads to an increase, but the effect is more pronounced for the bottom coil, especially at lower d_C values. This pattern reinforces the idea that smaller coil configurations exhibit stronger local dependencies, where coil placement relative to the detector height plays a crucial role in maintaining effective compensation. These results are consistent with previous studies that also reported vertical asymmetries and local effects in the compensation performance between top and bottom coils [17, 18]. It should be noted, however, that these observations are specific to the present configuration studied and may vary depending on the particular geometry and parameters of the setup considered.

These results indicate that, in the optimized system, the impact of failures becomes increasingly dependent on coil position, particularly for circular coils, reinforcing the notion that coil spatial distribution is crucial for maintaining effective compensation.

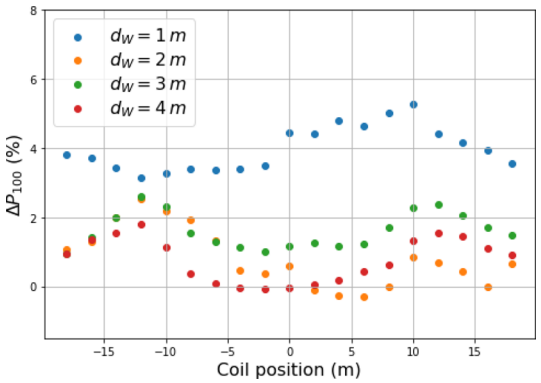

Fig. 22 Increase in P_{100} with the failure of each of the rectangular coils of the basic compensation system of a detector of $h = D = 40\,\text{m}$ and $d_C = 2\,\text{m}$ for different values of the distance between PMTs and coils d_W

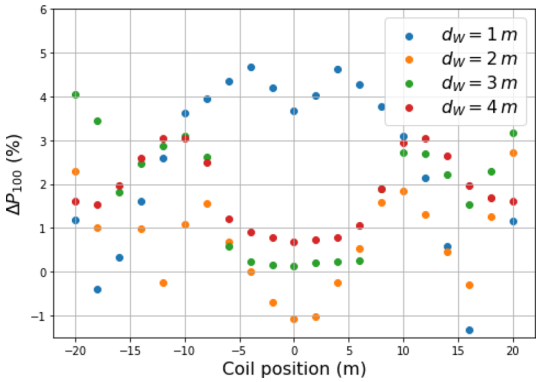

Fig. 23 Increase in P_{100} with the failure of each of the circular coils of the basic compensation system of a detector of $h = D = 40\,\text{m}$ and $d_C = 2\,\text{m}$ for different values of the distance between PMTs and coils d_W.

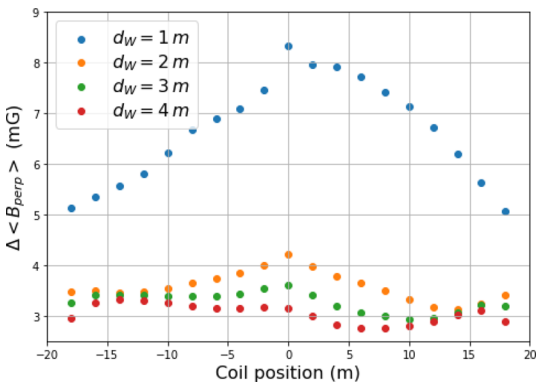

Fig. 24 Increase in $< B_{\text{perp}} >$ with the failure of each of the rectangular coils of the basic compensation system of a detector of $h = D = 40\,\text{m}$ and $d_C = 2\,\text{m}$ for different values of the distance between PMTs and coils d_W.

3.3 Distance to the PMTs effect

Finally, to complete this analysis, we perform a simulation to evaluate how the distance between PMTs and coils affects the impact of a coil failure on geomagnetic field compensation. Previous studies [17, 18] have highlighted the strong influence of this parameter, d_W, on the overall effectiveness of the compensation. In particular, it was observed that increasing d_W facilitates compensation, enhancing both its ease and effectiveness.

Figures 22, 23, 24 and 25 present the results of coil failure simulations of a basic compensation system of coils for a detector with $h = D = 40\,\text{m}$, with $d_C = 2\,\text{m}$ varying d_W are shown as an example of the effect of different values of d_W.

Table 5 presents the evaluation parameter values for the basic coil configuration without failures for each value of the distance between coils and PMTs considered are provided.

The effect of the distance between PMTs and coils, d_W, on the system's response to coil failures varies significantly depending on the coil configuration.

For rectangular coils, the overall trend remains consistent across all values of d_W, except for $d_W = 1\,\text{m}$, which shows some deviations. The increase in P_{100} is significantly larger for $d_W = 1\,\text{m}$, while for $d_W = 2,\ 3,\ 4\,\text{m}$ the trend remains consistent, without a clear preference for greater or smaller distances. Specifically, $d_W = 2\,\text{m}$ and $d_W = 4\,\text{m}$ yield the lowest increases, whereas $d_W = 3\,\text{m}$ results in the highest, though still lower than $d_W = 1\,\text{m}$. The minimum impact of a failure occurs when central

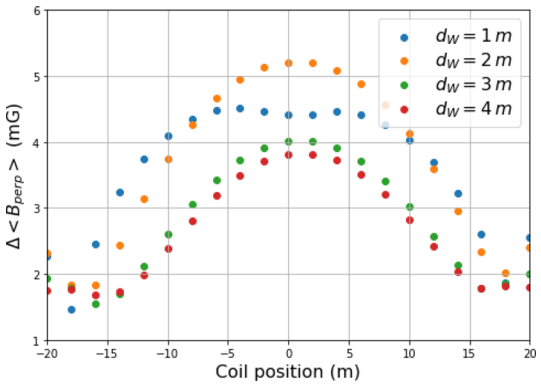

Fig. 25 Increase in $< B_{\text{perp}} >$ with the failure of each of the circular coils of the basic compensation system of a detector of $h = D = 40\,\text{m}$ and $d_C = 2\,\text{m}$ for different values of the distance between PMTs and coils d_W

Table 5 Values of P_{100} and $< B_{\text{perp}} >$ of the basic configuration of coils for a detector with $h = D = 40\,\text{m}$ and $d_C = 2\,\text{m}$

d_W	$P_{100}(\%)$	$< B_{\text{perp}} >$ (mG)
1 m	22.51	73.41
2 m	12.11	54.84
4 m	4.75	47.83
5 m	2.6	41.85

coils are lost, while two peaks are observed: one at 1/4 of the tank radius and another at 3/4. However, for $d_W = 1\,\text{m}$, the minimum is observed at one of these intermediate positions (1/4), while the maximum occurs at the coil positioned at 3/4.

For circular coils, the behavior changes. When $d_W = 1\,\text{m}$, the maximum increase in P_{100} occurs when a central coil fails, decreasing progressively toward the extremes. Again, $d_W = 1\,\text{m}$ displays a distinct pattern relative to the other cases. While failures in the central coils have the most severe effect, the failure of the extreme coils has the least impact on compensation compared to the other values of d_W. For $d_W = 2,\ 3,\ 4\,\text{m}$, the trend remains similar across all cases, with a smaller increase in P_{100} for central coil failures as d_W decreases, but a larger increase for failures in the extreme coils.

The behavior of $< B_{\text{perp}} >$ is simpler. For rectangular coils, the negative impact of a failure is highest for the central coil and decreases progressively toward the extremes, regardless of the d_W value. A clear trend emerges: the smaller d_W, the greater the increase in $< B_{\text{perp}} >$, with a particularly pronounced difference in the case of $d_W = 1\,\text{m}$, resulting in significantly greater increases compared to other values.

For circular coils, the trend remains similar but is slightly smoother. The maximum increase in $< B_{\text{perp}} >$ occurs when the central coil fails and decreases toward the extremes, although it slightly rises again when the uppermost and lowermost coils fail. Similarly, a greater d_W results in a reduced negative impact on compensation, with one exception: for $d_W = 1\,\text{m}$ and $d_W = 2\,\text{m}$, failures in the central coils exert a greater impact when $d_W = 2\,\text{m}$ case.

Overall, these results support the notion that increasing d_W tends to reduce the negative effects of coil failures on geomagnetic compensation. However, the extent to which this effect occurs depends on the coil shape and the specific location of the failure. **Furthermore, although increasing** d_W tends to reduce the impact of individual coil failures, a proper quantitative evaluation of its influence on the compensation metrics must account for the selected inter-coil distance d_C **,as addressed in Section** 3.1.

3.4 Coil set failure mitigation

In the previous sections, the impact of individual coil failures in the compensation system was examined to achieve a detailed understanding. However, in a real installation, coils are not individually connected. Given the large number of required coils, especially for larger detectors, they are grouped into sets, each powered by a single source. Consequently, a cable break or a failure in one coil results in the interruption of current in the entire set, resulting in a more pronounced impact on compensation compared to individual failures.

This section illustrates, using a practical case, the increased impact on compensation resulting from current flow interruption in one of these coil sets. Additionally, possible measures and design elements are proposed to minimize the impact of such an event should it occur.

For this purpose, an intermediate-sized detector with $h = D = 40\,\text{m}$ and $d_W = 2\,\text{m}$ is considered, along with its corresponding optimized coil-based compensation system. Table 3 indicates that the best compensation is obtained with a distance between coils of $d_C = 2\,\text{m}$. In this configuration, the optimized layout includes four additional turns on the circular coils at the upper and lower ends ($z = \pm 20\,\text{m}$) and one coil of smaller radius ($r = 14\,\text{m}$) at both positions.

Table 6 Distribution in sets of the circular coils of the optimized compensation system for a detector of $h = D = 40\,\text{m}$ with $d_W = 2\,\text{m}$

Set	Coil positions (m)
A	− 20
B	− 18, − 16, − 14, − 12
C	− 10, − 8, − 6, − 4
D	− 2, 0, 2
E	4, 6, 8, 10
F	12, 14, 16, 18
G	20

Table 7 Distribution in sets of the rectangular coils of the optimized compensation system for a detector of $h = D = 40\,\text{m}$ with $d_W = 2\,\text{m}$

Set	Coil positions (m)
H	− 18, −16, − 14, − 12
I	− 10, − 8, − 6, − 4
J	− 2, 0, 2
K	4, 6, 8, 10
L	12, 14, 16, 18

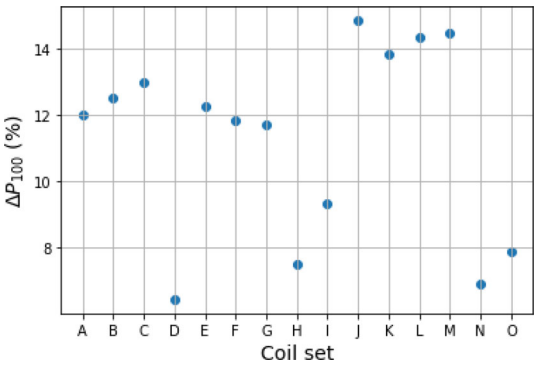

Fig. 26 Increase in P_{100} with the failure of each coil set of the optimized compensation system of a detector of $h = D = 40\,\text{m}$, $d_W = 2\,\text{m}$ and $d_C = 2\,\text{m}$

Having a separate power supply for each coil would be excessively costly and energy-inefficient. Accordingly, the current flowing through all coils of the same type (rectangular or circular) is assumed to be identical throughout this study. As a result, these coils must be grouped into different sets, each powered by a single source.

Tables 6 and 7 present the proposed coil distribution across different sets. Each set comprises four coils, except for the central set in both circular and rectangular configurations, as well as the first and last sets of circular coils.

The size of the central sets was reduced based on the findings in Figs. 18 and 20, which show that central coil failures have the most significant negative impact on $< B_{\text{perp}} >$. This is not the case for P_{100}, but since it has been proven that $< B_{\text{perp}} >$ has a greater impact on the loss of detection efficiency [18], minimizing this parameter is prioritized.

Additionally, sets A and G consist exclusively of circular coils, both top and bottom, as the number of turns is increased and the smaller coil is also included.

Figures 26 and 27 illustrate the increase in both P_{100} and $< B_{\text{perp}} >$ caused by current flow interruption in each of the defined sets within the coil-based compensation system. As expected, the negative impact of the failure of one of these sets is significantly higher than that of an individual coil, compared to the results in Figs. 14 to 20, reaching a maximum increase in $\Delta P_{100} = 21.46\%$ in case of failure of set K, composed of rectangular coils, and of $\Delta B_{\text{perp}} = 41.57\,mG$ in case of failure of set I, also of rectangular coils.

In both parameters, the increase is more pronounced for coil sets positioned farther from the ends, with a drop in the central set. This set was specifically designed with three coils to minimize the impact of a potential failure, which would otherwise have the most severe impact.

3.4.1 Fail-safe connection proposal

If a coil fails or breaks, interrupting the current flow, the entire set will be disconnected. This significantly affects geomagnetic compensation, reducing detection efficiency. A similar issue was observed in the Super-Kamiokande experiment, where coil failures, likely caused by water connection corrosion, led to measurable performance degradation [19]. In that case, some of the coil connections were located underwater, as shown in Fig. 28, making them inaccessible for repair. As a result, when a failure occurred

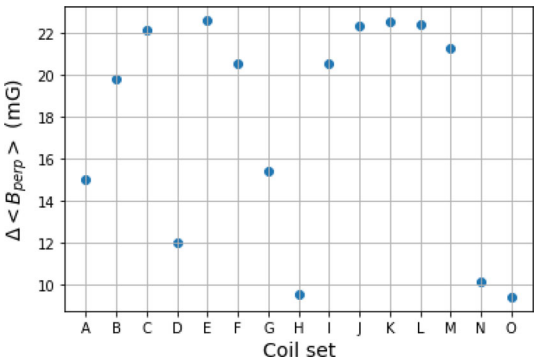

Fig. 27 Increase in $< B_{\text{perp}} >$ with the failure of each coil set of the optimized compensation system of a detector of $h = D = 40\,\text{m}$, $d_W = 2\,\text{m}$ and $d_C = 2\,\text{m}$

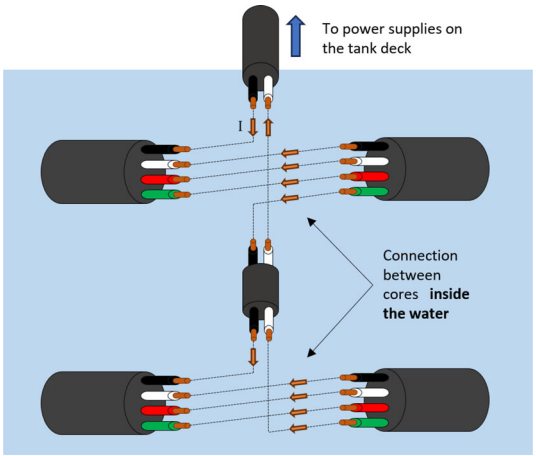

Fig. 28 Diagram of underwater connections as the ones used in Super-Kamiokande experiment

in one of these junctions, the entire coil set had to be disconnected until a full replacement could be performed, further exacerbating the impact on the experiment.

To reduce the impact of such failures, a more resilient connection system is proposed. Instead of relying on a single-core cable for each coil, multi-core cables can be employed. In particular, four-core cables are proposed as an effective solution, as they allow the current to be evenly distributed among the four conductors. This not only reduces the current per conductor, minimizing potential overheating or localized damage, but also facilitates partial recovery in case of failure. If one of the cores is damaged, the remaining three can still conduct current, allowing the set to remain at least partially operational.

For this strategy to be effective, the inter-core connections must be relocated to an accessible position above water, reducing the likelihood of corrosion and simplifying maintenance. The proposed four-core cable connection system is illustrated in Fig. 29. If a coil conductor breaks (e.g., the blue core in Fig. 30), an external bypass can be established at the surface, rerouting current through an alternate core (e.g., bridging the black and red conductors). This ensures that the current still flows through the set via the remaining three cores, maintaining proper coil compensation system performance.

Although the proposed fail-safe wiring system offers practical advantages, its implementation must be tailored to the specific constraints of each detector. The current proposal is intended as a flexible design concept that can be adapted to different experimental contexts and is supported by its successful implementation in large-scale detectors such as Hyper-Kamiokande.

4 Conclusions

The accurate compensation of the geomagnetic field is crucial for ensuring the optimal performance of Cherenkov neutrino detectors, as the field can significantly affect the efficiency of photomultiplier tubes (PMTs). While active compensation using current-carrying coils has proven to be a flexible and effective approach, its reliability hinges on the proper functioning of the coils. Failures in these coils can compromise compensation efficiency, potentially reducing the detector's overall performance. Despite its importance, the effect of coil malfunctions has received limited attention, highlighting the need for this study to understand and mitigate their impact.

The results of this study show that coil failures result in a higher residual perpendicular magnetic field, negatively affecting PMT performance. The impact is not uniform across all coils, with failures in central coils generally causing the most significant degradation. This effect is particularly pronounced for larger coil spacings, making compensation more vulnerable to local disruptions.

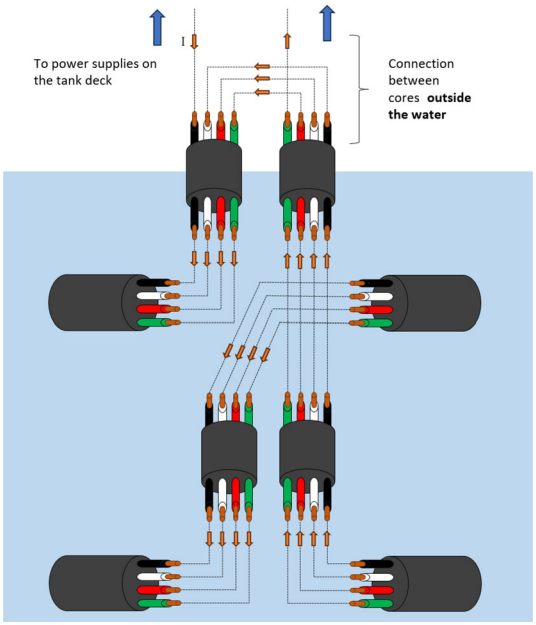

Fig. 29 Out of water connections proposed with four-core cables for the coil safe system

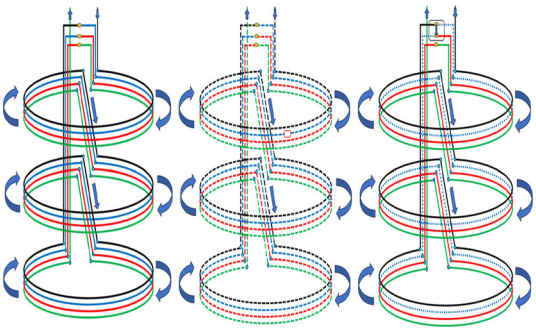

Fig. 30 Example of out of water fail-safe system for circular coils

However, in larger detectors, although compensation is more challenging, sensitivity to individual coil failures is slightly reduced due to the overall field distribution.

The impact of coil failures has also been examined in a more refined compensation system, incorporating additional circular coils at the upper and lower ends of the detector. The results confirm that although this enhanced design improves overall compensation efficiency, it remains susceptible to coil failures, particularly in the central region. However, compared to simpler configurations, the optimized system exhibits a more position-dependent response to failures in the case of circular coils, whereas the response remains nearly unchanged for the rectangular ones. Additionally, the study of the influence of the distance between PMTs and coils has demonstrated that larger separations generally facilitate compensation and reduce the negative impact of coil failures. The results indicate that for sufficiently large distances, the system becomes more robust, while very small distances lead to stronger local field variations, amplifying the effects of individual coil failures.

In addition to optimizing coil placement and configuration, this study also introduces a fail-safe connection system aimed at mitigating the effects of coil failures. The proposed design incorporates multi-core cables rather than traditional single-core cables and relocates critical connections above water. This modification allows for partial current redistribution in the event of a coil failure, maintaining compensation effectiveness without requiring an immediate coil replacement. Unlike conventional underwater connection schemes, which hinder repairs and necessitate full coil disconnection, this new approach ensures higher stability and system resilience.

These findings offer key insights into the design of coil-based geomagnetic compensation systems for large-scale neutrino detectors. By incorporating optimized configurations and fail-safe mechanisms, future detectors can achieve more reliable compensation, reducing efficiency losses, even in the presence of coil malfunctions. Future studies could refine the proposed fail-safe system and evaluate its performance in experimental settings.

Acknowledgments. This research paper was supported by Boosting Ingenium for Excellence (BI4E) project, funded by the European Union's European Union's HORIZON-WIDERA-2021-ACCESS-05-01-European Excellence Initiative under the Grant Agreement No. 101071321. It has also been developed with financial support from the grant by the MRR-22-MCINN-HKK-CANFRANC project founded by MICINN and FICYT regional plans. SLS, MLS and JDS acknowledge financial support from project PID2022-139198NB-I00. LB acknowledges financial support from the PID2021-125630NB-I00 project

funded by MCIN/AEI/10.13039/501100011033/FEDER, UE. FJDC acknowledges financial support from the PID2021-127331NB-I00 project funded by MCIN/AEI/10.13039/501100011033/FEDER, UE.

Funding Open Access funding provided thanks to the CRUE-CSIC agreement with Springer Nature.

Data availability statement The datasets generated during and/or analyzed during the current study are available from the corresponding author on reasonable request. The manuscript has associated data in a data repository.

References

1. Takaaki Kajita, Rep. Prog. Phys. **69**, 1607 (2006). https://doi.org/10.1088/0034-4885/69/6/R01
2. K. Scholberg, Ann. Rev. Nuclear Particle Sci. (2012). https://doi.org/10.1146/annurev-nucl-102711-095006
3. K. Abe, et al., *Hyper-Kamiokande Design Report*. 28 Nov 2018. Available: arXiv:1805.04163v2 [physics.ins-det]
4. Zh.-A. M. Dzhilkibaev et al., Phys.-Usp.58495 2015.https://doi.org/10.3367/UFNe.0185.201505j.0531
5. B. Abi et al., JINST **15**, T08008 (2020). https://doi.org/10.1088/1748-0221/15/08/T08008
6. C.W. Walter, The Super-Kamiokande Experiment. Neutrino Oscillations: Present Status and Future Plans, J. Thomas and P. Vahle editors, World Scientific Publishing Company (2008). https://doi.org/10.1142/9789812771971_0002
7. J. Collaboration, JUNO Physics and Detector. Progr. Particle Nuclear Phys. (2021). https://doi.org/10.1016/j.ppnp.2021.103927
8. J. Ahrens et al., IceCube preliminary design document. Astropart. Phys. **20**, 507 (2001)
9. A. Margiotta, Nuclear instruments and methods in physics research section a: accelerators. Spectrom. Detect. Assoc. Equip. **766**, 83–87 (2014). https://doi.org/10.1016/j.nima.2014.05.090. (**ISSN 0168-9002.**)
10. G. Bellini, Ann. Rev. Nuclear Particle Sci. **74**, 369–388 (2024). https://doi.org/10.1146/annurev-nucl-102622-021701
11. A. Bellerive et al., The sudbury neutrino observatory. Nuclear Phys. B Proc. Suppl. **221**, 1–15 (2011). https://doi.org/10.1016/j.nuclphysb.2016.04.035
12. J. Bian, The NOvA Experiment: Overview and Status. Meeting of the American Physical Society Division of Particles and Fields (2013) . https://doi.org/10.48550/arXiv.1309.7898
13. S. Aiello et al., Influence of the Earth's magnetic field on large area photomultipliers. IEEE Trans. Nuclear Sci. **59**(4), 1259–1267 (2012). https://doi.org/10.1109/TNS.2012.2189245
14. F.P. An et al., Observation of electron-antineutrino disappearance at Daya bay. Phys. Rev. Lett. **108**, 171803 (2012)
15. A. Ianni, G. Korga, G. Ranucci, O. Smirnov, A. Sotnikov, INFN-TC-00-18 (2000). https://doi.org/10.15161/oar.it/1448986128.29
16. T. Tomiya, *Investigation of the Impact of Magnetic Field on 50 cm Diameter Photomultiplier Tubes for Hyper-Kamiokande* (The University of Tokyo, JFY, Tokyo, 2022)
17. S.R. Cabo et al., Magnetic shielding for particle detection. Eur. Phys. J. Plus **138**(903), 2023 (2023). https://doi.org/10.1140/epjp/s13360-023-04520-1
18. S.R. Cabo et al., *Optimization of Geomagnetic Shielding Based on Detection Efficiency* https://doi.org/10.1140/epjp/s13360-025-06230-2
19. M. Posiadala-Zezula, XXXI International Conference on Neutrino Physics and Astrophysics, Milan, Italy, 17-22 June (2024)
20. G. Zhang et al., Study of active geomagnetic shielding coils system for JUNO.arXiv:2106.09998 [physics.ins-det] 23 Nov (2021)
21. L.J. Wen et al., Nuclear Inst. Methods Phys. Res. A **947**, 162766 (2019). https://doi.org/10.1016/j.nima.2019.162766
22. S. Fukuda et al., Volume 501, Issues 2–3, 1 April 2003, pp. 418–462. https://doi.org/10.1016/S0168-9002(03)00425-X
23. S. Katoch, S.S. Chauhan, V. Kumar, Multimed. Tools Appl. **80**, 8091–8126 (2021). https://doi.org/10.1007/s11042-020-10139-6